FLog: Automated Modeling of Link Quality for LoRa Networks in Orchards

KANG YANG, University of California Merced, Merced, United States
YUNING CHEN, University of California Merced, Merced, United States
WAN DU, University of California Merced, Merced, United States

LoRa networks have been deployed in many orchards for environmental monitoring and crop management. An accurate propagation model is essential for efficiently deploying a LoRa network in orchards, e.g., determining gateway coverage and sensor placement. Although some propagation models have been studied for LoRa networks, they are not suitable for orchard environments, because they do not consider the shadowing effect on wireless propagation caused by the ground and tree canopies. This article presents *FLog*, a propagation model for LoRa signals in orchard environments. *FLog* leverages a unique feature of orchards, i.e., all trees have similar shapes and are planted regularly in space. We develop a three-dimensional model of orchards. Once we have the location of a sensor and a gateway, we know the media that the wireless signal traverses. Based on this knowledge, we generate the First Fresnel Zone (FFZ) between the sender and the receiver. The intrinsic path loss exponents of all media can be combined into a classic Log-Normal Shadowing model in the FFZ. Extensive experiments in almond orchards show that *FLog* reduces the link quality estimation error by 42.7% and improves gateway coverage estimation accuracy by 70.3%, compared with a widely used propagation model. The source codes and dataset are released at https://github.com/ycucm/Flog.

CCS Concepts: • **Networks** → **Wide area networks**; *Network measurement;*

Additional Key Words and Phrases: Low-power wide-area networks, LoRa, link quality, signal propagation model, first fresnel zone

ACM Reference Format:
Kang Yang, Yuning Chen, and Wan Du. 2025. FLog: Automated Modeling of Link Quality for LoRa Networks in Orchards. *ACM Trans. Sensor Netw.* 21, 2, Article 22 (March 2025), 28 pages. https://doi.org/10.1145/3718741

1 Introduction

The orchard crop is a significant contributor to the economy in California, generating over 8.96 billion dollars in profit in 2021 [60]. Smart orchard management, such as smart irrigation [12, 17], tree health monitoring [13, 49], and pest control [43], is crucial for improving yield and minimizing

---

Kang Yang and Yuning Chen contribute equally to the article.

This publication was prepared with the support of a financial assistance award approved by the Economic Development Administration, Farms Food Future. It was also supported in part by NSF Grant #2239458, a UC Merced Fall 2023 Climate Action Seed Competition grant, and a UC Merced Spring 2023 Climate Action Seed Competition grant. Any opinions, findings, and conclusions expressed in this material are those of the authors and do not necessarily reflect the views of the funding agencies.

Authors' Contact Information: Kang Yang, University of California Merced, Merced, California, United States; e-mail: kyang73@ucmerced.edu; Yuning Chen, University of California Merced, Merced, California, United States; e-mail: ychen372@ucmerced.edu; Wan Du (Corresponding author), University of California Merced, Merced, California, United States; e-mail: wdu3@ucmerced.edu.

ACM 1550-4859/2025/03-ART22
https://doi.org/10.1145/3718741

cost [31, 57]. All these applications need to deploy a large number of sensors across the orchards, e.g., tens or even hundreds of acres. LoRa is a promising solution with a communication range of several miles, allowing gateways to receive sensor data in a large field [10, 21, 25, 47]. However, this range is only achievable in free space [9, 22], which is rarely found in orchards.

Our preliminary experimental results reveal that in an almond orchard, LoRa signals can only be reliably transmitted up to 140 m with a **Spreading Factor (SF)** of 10; whereas LoRa signals with the same hardware and transmission parameters can reach a communication distance of 2 km in free space. In orchards, LoRa sensor nodes are typically installed close to the ground, under the tree canopy. Meanwhile, LoRa gateways are often placed on towers of 6–10 m, because there are no high buildings on farms and it is expensive to construct taller towers. As a result, the energy of wireless signals may be absorbed and reflected by the ground, which can affect the LoRa signal propagation. In addition, the wireless signal from a sensor node must penetrate through the canopies of multiple trees to reach a gateway.

In this article, we study the propagation modeling [40] of LoRa signals in orchard environment, which requires to estimate the attenuation of wireless signals as they propagate through all media between the transmitter and the receiver, such as air and tree canopy. Although two propagation models [16, 35] for LoRa have been developed for large-scale urban scenarios, they cannot be used in orchards. For example, for a sensor node in orchards, its signal propagation varies significantly across different directions, since the signal traverse different distances in canopies. In addition, several foliage propagation models [27, 45, 62] have been studied for wireless signals passing through trees. They are developed for high-frequency channels (e.g., 5 GHz in satellite communications) but not applicable to LoRa links. The propagation characteristics of low-frequency LoRa signals are different from high-frequency signals, and these foliage propagation models do not consider the impact of the ground on LoRa signal propagation.

To study the characteristics of LoRa signal propagation in orchards, we conduct a series of experiments using a gateway and a LoRa sensor node. The latter is deployed at different locations for experiments (Section 4.1 for details). Based on our experimental results, we made three observations. (1) If the sender and the receiver are both under trees, then the link quality of the visual **line-of-sight (LoS)** path is worse than that of non-visual LoS paths. When a wireless signal passes through a tree, it may penetrate, scatter (i.e., reflected or refracted), or diffract around the tree. This power loss is known as shadowing effect, which needs to be analyzed from a three-dimensional (3D) perspective. (2) Due to the long wavelength of LoRa signals, wireless signals can easily diffract from tree trunks and branches. (3) The low installation height of LoRa sensor nodes means that the ground has an apparent shadowing impact on signal propagation.

Based on the observations above, this article presents *FLog*, a wireless signal propagation model designed for LoRa links in orchards. It is inspired by the regular layout of orchards, where all trees are aligned and have a similar shape and canopy density, as they are planted and pruned at the same time. The shape of a tree can be modeled by a few parameters, including tree height, trunk height, and canopy width. The layout of an orchard can be modeled by the shape of its trees and the spacing distances between rows and columns. Given the locations of a sensor node and a gateway, we can leverage our 3D orchard model to study the complex shadowing effect that the wireless signal will experience from the sensor node to the gateway. Based on the shadowing effect analysis, our wireless propagation model can calculate the attenuation that the signal will have as it travels through the air and tree canopies. Combining the predefined transmission settings, including antenna gains and transmission power, we can calculate the strength of the received LoRa signal.

FLog adopts the **First Fresnel Zone (FFZ)** to capture the complex shadowing effect caused by tree canopies and ground in orchards. FFZ is a 3D ellipsoid region with two focus points located at the node and the gateway. This zone carries most of the signal energy received by the receiver.

Different links have their unique portions of the wireless transmission media in their FFZs. To calculate the portion of each medium for a transmission pair, we perform numerical sampling in the FFZ. Each sampling point may encounter free space, trees, or the ground. The portions of sampling points in each medium over the total number of points are used as weights for profiling the shadowing effect. These weights are used to combine the intrinsic **path loss exponent (PLE)** of each transmission medium, resulting in the final PLE of the classic Log-Normal Shadowing model in the FFZ.

Beside the weights, we also need to determine the intrinsic PLEs for each medium in *FLog*. We obtain these parameters by fitting the collected packets' signal strength using the nonlinear least square algorithm [51]. Furthermore, we adapt these parameters to environmental variation based on a few recently received packets.

To demonstrate the applications of our propagation model, we use *FLog* to determine gateway coverage. A LoRa node is considered to be covered by a gateway if the **Packet Delivery Ratio (PDR)** exceeds 80% [74, 76]. The PDR is computed using a **Bit Error Ratio (BER)** model [20], with inputs of **Signal-to-Noise Ratio (SNR)** and SF. We use *FLog* to estimate the SNR for any LoRa nodes and a gateway and thus the coverage of that gateway under different transmission settings.

Extensive experiments have been conducted in two almond orchards and one walnut orchard. The results show that *FLog* can reduce path loss estimation errors by up to 42.7% compared to the Log-Normal Shadowing model. Additionally, *FLog* provides more accurate PDR estimation for gateway coverage, reducing the estimation error by 70.3% compared to the Log-Normal Shadowing model. Numerical analysis shows that *FLog* can facilitate scheduling fewer gateways while maintaining reliable link quality.

In summary, this article makes three major contributions:

- We study the propagation modeling problem of wireless LoRa signals in orchards and explain why path loss models only considering the direct ray blockage are unsuitable for the orchard scenario.
- We propose *FLog*, a novel interpretable propagation model for LoRa networks in orchards. It leverages the first Fresnel zone theory and the regular tree layout of orchards to model the complex shadowing effect caused by tree canopies and the ground with minimal overhead.
- Extensive experiments demonstrate the effectiveness of *FLog*. A gateway coverage study shows the usability of *FLog*. We release *FLog* source code on GitHub [4].

2 Background and Motivation

After a brief introduction to the basic LoRa concepts and the Log-Normal Shadowing model, we conduct experiments to study LoRa links in free space and orchards.

2.1 LoRa Primer

The LoRa adopts **Chirp Spread Spectrum (CSS)** modulation to facilitate long-distance and low-power communication [29, 39, 69, 70].

The sensory data undergoes a series of encoding operations at the sender side to improve its over-the-air resilience. These operations consist of **Forward Error Correction (FEC)** encoding, whitening, diagonal interleaving, and gray mapping, and are followed by CSS modulation of the encoded data into multiple symbols. Each symbol represents an integer from 0 to $2^{SF}-1$, where SF determines the number of bits in each symbol. To modulate a symbol, a base chirp with an initial frequency is shifted by a step of $BW/2^{SF}$, where BW is the frequency channel bandwidth.

At the receiver side, LoRa performs demodulation and decoding. Demodulation identifies a symbol's value by measuring its chirp's initial frequency, and the resulting signal is subjected to FFT to obtain the amplitude spectrum of each received symbol. Each frequency bin corresponds to a possible symbol value, and the symbol value with the highest amplitude is identified by the frequency bin. The recognized symbols are then concatenated into a binary sequence that undergoes Gray demapping, deinterleaving, and dewhitening in sequence. The original sensory data can be obtained by FEC decoding.

Frequency Band: LoRa operates on license-free radio frequency bands, such as 915 MHz in North America. It can transmit over long distances of several miles or more in rural areas. In contrast, high-frequency bands such as 2.4 GHz or 5 GHz used by WiFi have a short communication range, typically limited up to 45 m indoors [19, 64]. This short communication distance makes it difficult to provide coverage for orchards that span several acres.

Expected Signal Power (ESP): LoRa defines the ESP to quantify the received signal strength [16, 34, 35], which is derived from the measured **Received Signal Strength Indicator (RSSI)** and SNR,

$$\mathrm{ESP} = \mathrm{RSSI} + \mathrm{SNR} - 10 \cdot \log_{10}\left(1 + 10^{0.1 \cdot \mathrm{SNR}}\right), \tag{1}$$

where the unit of ESP and RSSI is decibel-milliwatts (dBm) and the unit of SNR is decibels (dB). The RSSI and SNR are reported from the LoRa gateway for each received packet.

2.2 Log-Normal Shadowing Model

The Log-Normal Shadowing model is widely used to predict the received signal power [46]. The ESP of a received packet, P_{rx}, is calculated as follows [46]:

$$P_{rx} = P_{tx} + G_{tx} + G_{rx} - PL, \tag{2}$$

where P_{tx} represents the transmission power in decibel-milliwatts, G_{tx} and G_{rx} denote the transmitting and receiving antenna gains in decibels relative to isotropic (dBi), respectively. The last term PL is the path loss [55] in decibels and can be calculated via the Log-Normal Shadowing model [46],

$$PL(d) = \overline{PL}(d_0) + 10 \cdot n \cdot \log\left(\frac{d}{d_0}\right) + X_\sigma, \tag{3}$$

where the distance between a LoRa node and a gateway is denoted as d in meters, n is the PLE, and X_σ is a zero-mean Gaussian distribution with a standard deviation of σ. The reference path loss $\overline{PL}(d_0)$ is obtained from field measurements at a reference distance of d_0, where d_0 is normally set to 1 m [16]. Based on our collected packets, we obtained an average $\overline{PL}(d_0)$ of 78.59 dBm.

When considering a specific distance, the model represents the path loss as a Gaussian distribution with a mean of $\overline{PL}(d_0) + 10n\log\left(\frac{d}{d_0}\right)$ and a standard deviation of σ. As the model produces a distribution, its accuracy cannot be assessed against a single measurement. Instead, we use the mean as the model's predictive result, enabling the calculation of the absolute error relative to the measured signal strength. In the following, unless specified otherwise, the output of the Log-Normal Shadowing model is assumed to be the mean value.

2.3 Free Space Scenario

We conducted an experiment to measure the LoRa link quality in the free space. Figure 1(a) shows that a LoRa node is placed at four locations with distances of 0.5, 1.0, 1.5, and 2 km. The nodes and gateway are installed on two poles with heights of 6 and 10 m, respectively. The nodes transmitted packets periodically with SF10, $P_{tx} = 14$ dBm, a bandwidth of 125 kHz, and a coding rate of 4/5.

Figure 2(a) depicts the experimental results. Even at a distance of 1.5 km, the link's SNR remains above the receiving sensitivity threshold (i.e., −7.5 dB for SF7). This indicates that LoRa nodes can transmit packets using SF7 at distances of up to 1.5 km in free space. However, the SNR at

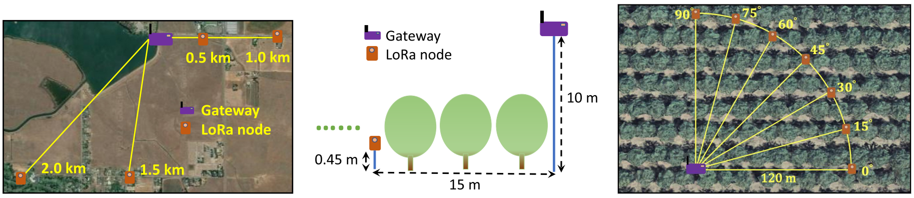

(a) Free space scenario (b) A typical scenario in orchards (c) Nodes at seven directions

Fig. 1. The deployment layout of the almond orchard and illustration for different directions.

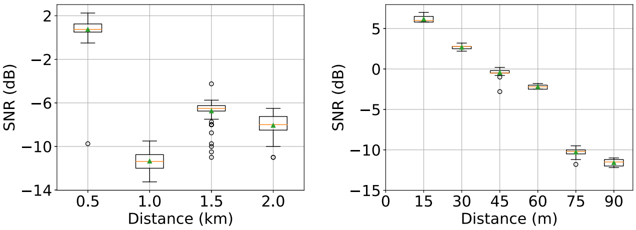

(a) Free space scenario (b) The orchard scenario

Fig. 2. The measured link quality (SNR) in the free space and almond orchard.

a distance of 1.0 km is lower than that at 1.5 and 2.0 km, primarily because buildings and trees obstruct the propagation path, as illustrated in Figure 1(a). This highlights the significant impact of blockages on link quality.

2.4 Orchard Scenario

Figure 1(c) depicts an almond orchard where trees are organized tidily to facilitate uniform allocation of sunlight, water, and soil nutrients. LoRa nodes and the gateway are deployed in orchards as shown in Figure 1(b). The nodes are typically positioned on the ground or attached to the main branches, measuring data related to soil and tree health. The installation height is usually between the ground and the canopy, less than 1.2 m (e.g., 0.45 m in our implementation). Meanwhile, the gateway is mounted on top of a pole or tower (e.g., 10 m in our implementation), providing long communication coverage, as shown in Figure 11. Therefore, the signals from sensor nodes normally pass through three media: free space, the ground, and trees in orchards.

2.4.1 Short Communication Distance. We conducted an investigation of link quality in an almond orchard. The position of the gateway is fixed in the center between two adjacent almond trees in a row. We then move the locations of LoRa nodes in the row, the communication distance between the node and gateway ranges from 15 to 90 m with a step of 15 m. The transmission settings were identical to those outlined in Section 2.3. From Figure 2(b), we observed a significant reduction in communication: At only 90 m, the SNR was −12.0 dB. As a result, SF10 was necessary for a reliable communication distance of 90 m. Conversely, SF7 was suitable for distances of 1.5 km in free space. By fitting our collected data, we found that the PLE in the almond orchard was 2.95. This value is larger than that of free space, indicating a shorter communication distance, and reflects the high path loss in the orchard caused by tree blockage.

2.4.2 Large Deviation at Different Directions. We then measured the received signal strength in seven directions, ranging from 0° to 90° in 15° increments for a fixed distance, as depicted in

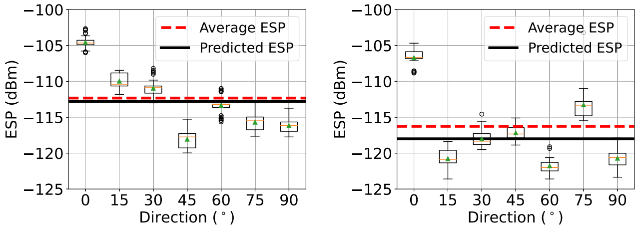

(a) Distance = 80 m (b) Distance = 120 m

Fig. 3. The measured link quality (ESP) at different directions for two communication distances.

Table 1. Notations Used in This Article

Notations	Meaning
ESP	Expected signal power.
PLE	The path loss exponent (PLE) of a LoRa link.
α	The PLE when the space is filled with air.
β	The PLE when the space is filled with foliage.
γ	The PLE when the space is filled with the ground.
P_{open}	The portion of free space within the propagation path.
$P_{foliage}$	The portion of the foliage within the propagation path.
P_{ground}	The portion of the ground within the propagation path.
p_{gap}	The distance between two adjacent sampling planes.
N_{ref}	The number of sampling points of the first sampling plane.

Figure 1(c). Figure 3 shows the ESP of the received signal at different directions for communication distances of 80 and 120 m. The dotted red line represents the average ESP in seven directions for one distance. The results indicate a significant variation in the signal ESP across different directions, with discrepancies of up to 13 dBm, such as −105 dBm vs. −118 dBm at 0° and 45°.

According to Equation (3), the Log-Normal Shadowing model predicts a mean ESP value for a given distance, as shown by the black line in Figure 3. Although the predicted ESP with the Log-Normal Shadowing model is close to the average ESP, with errors of less than 1 dBm, the overall ESP error across all the collected data can exceed 4 dBm due to the significant deviation in signal strength across different directions. This finding motivates us to develop a new propagation path loss model that can account for the variation in signal strength across different directions.

3 Strawman Solution

This section develops a strawman solution to model link quality in orchards. We first build an orchard 3D profile. Using this profile, we specify the PLE of a Log-Normal Shadowing model. Table 1 summarizes the notations used in this article.

3.1 3D Modeling of Orchards

Abstracting One Tree: Botanists have developed several detailed tree models based on physiological knowledge [53]. However, these models require precise measurements of the shapes of trunks, branches, and leaves for all trees in an orchard, which is a labor-intensive process. We adopt a simple solution proposed by Torrico et al. [58]. It profiles the trunk as a cylinder and abstracts the crown as an ellipsoid with varying horizontal and vertical radii, as shown in Figure 1(b). To create a profile of a tree, we need to measure its height, trunk height, canopy width, and trunk radius.

Abstracting an Orchard: Orchards typically have a uniform layout, with trees being planted at the same time of year and exhibiting similar shapes. To analyze an orchard, we adopt a Cartesian coordinate system with the x-axis and y-axis representing the directions along and across rows, respectively. We also measure the distances between adjacent rows and adjacent trees in one row, which determine the positions of all trees in the Cartesian coordinate system.

Therefore, by adding two parameters, we can extend tree modeling to orchard modeling. With all of these parameters as input, we can reconstruct the orchard as 3D shapes, which can be translated into point clouds. Specifically, given the position of any point, we can determine whether it falls within the foliage or not.

3.2 Adapting PLE with Line Shadowing

Figure 4 depicts the signal propagation path between a LoRa node and a gateway, where the path is viewed as a direct line. The path includes both free space and foliage portions, which can have different shadowing effects on the signals. Thus, it is intuitive to consider these two parts separately.

To achieve this, we calculate the free space and foliage portions along the propagation path's direct line, denoted as P_{open} and $P_{foliage}$, respectively. To calculate the foliage portion $P_{foliage}$, we equally split the direct line into numerous points. If a point is in the tree, then the foliage points increase by 1; otherwise, the free space points increase by 1. Finally, the foliage portion $P_{foliage}$ is obtained by dividing the foliage points by the total number of points, which is similar to the free space portion calculation. The sum of these portions should be equal to 1.

As free space and foliage have different shadowing effects, they have different PLEs in the Log-Normal Shadowing model. To account for this heterogeneity, we propose an adaptive PLE calculation approach. This involves separating the path into two types of media (free space and foliage) and then recombining them together,

$$PLE_{comb} = P_{open} \cdot \alpha + P_{foliage} \cdot \beta, \tag{4}$$

where α denotes the free space PLE and β is the PLE when the space is filled with foliage. To determine the values of α and β, we perform a least square fitting on a collected dataset. The final PLE_{comb} is a compromise between the two values. For example, if $P_{open} = 1$, then it means that no trees are present and the path can be treated as free space. Once we have determined the PLE_{comb}, we can calculate the total path loss using the Log-Normal Shadowing model.

From experimental results in Figure 20(c), the strawman solution (marked as "LLog") can provide different estimations in different directions, but this model underestimates or overestimates the path loss in some directions. The possible reason is that we modeled the propagation path as a direct line. But the surrounding area also plays a role for the signal propagation.

4 The Design of *FLog*

This section presents tree validations via the empirical analysis of the LoRa signal propagation in orchards. We then introduce a path loss model based on the FFZ.

4.1 Empirical Analysis of LoRa Signal Propagation

To design a path loss model for orchards, it is crucial to understand how the signal propagates within this environment. Therefore, we conducted three preliminary experiments to investigate the LoRa signal propagation in orchards.

4.1.1 Visual Line-of-Sight Path. At frequencies around 900 MHz, the wavelength facilitate diffraction around obstacles. This implies that radio waves can "bend" and may not necessarily demand a direct line of sight [23]. We have conducted experiments to validate this assertion.

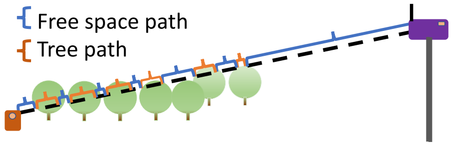

Fig. 4. The illustration of the strawman solution.

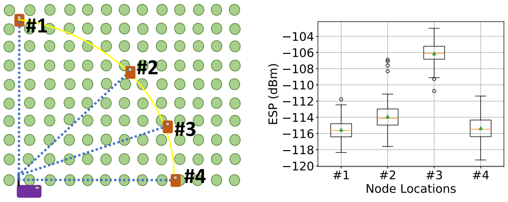

(a) Experimental Settings (b) ESP for four locations

Fig. 5. The visual and non-visual LoS paths.

Figure 5(a) shows the experimental setup where a gateway is positioned at the lower-left corner, and four different locations are selected to place LoRa nodes in varying directions but with the same communication distance of 60 m between the gateway and nodes. The gateway and nodes are placed at a height of 0.45 m. Locations #1 and #2 have the visual LoS propagation path, while locations #3 and #4 have the non-visual LoS path that passes through two and ten trunks, respectively. At each location, a LoRa node transmits packets periodically for 3 min with an interval of 1.5 s.

According to Figure 5(b), location #3 with the non-visual LoS path achieves the highest ESP, which is even higher than the visual LoS path (i.e., location #1 and #2). Furthermore, despite having ten trunks in location #4, this non-visual LoS path still attains a comparable ESP to the visual LoS path at locations #1 and #2. In summary, we conclude as follows:

Observation 1. *In orchards, the surrounding environment around the visual LoS path plays a pivotal role in determining the strength of LoRa signal.*

4.1.2 Diffracted Signal Strength. Diffraction refers to the propagation of waves behind an obstruction.

Figure 6(a) shows the setup of experiments, where the green circles represent tree trunks. In both settings #1 and #2, there is one trunk located between the nodes and the gateway. The difference is that in setting #2, the trunk is positioned very close to the gateway antenna, resulting in significantly weaker diffracted waves [41, 72].

Although setting #3 has five trunks between the gateway and node, resulting in weaker penetrating signal power, Figure 6(b) shows that its signal power is similar to that of setting #1. Furthermore, we can see that setting #2 exhibits the lowest signal strength, with a difference of more than 6 dBm compared to setting #1 and 4 dBm compared to setting #3. This leads us to the second validation as follows:

Observation 2. *Comparing setting #1 with #2, diffraction plays a crucial role in LoRa signal propagation. Comparing setting #1 with #3, the signal power from diffraction outweighs the power transmitted in the direct line.*

4.1.3 Ground Absorption. Signal propagation in orchards can be impacted by the low height of nodes, resulting in the absorption of signal energy by the ground. To investigate this effect on signal power, we conducted experiments in a free sand region without any obstacles. The experiments involved fixing the horizontal distance at 100 m and maintaining the sensor height at 0.45 m while varying the gateway height to 0.5, 1, and 1.5 m, as illustrated in Figure 7(a). The results, shown in Figure 7(b), reveal that increasing the gateway height leads to an increase in the received signal power.

Observation 3. *When the sender and receiver are in close proximity to the ground, a significant portion of the signal power can be absorbed by the ground.*

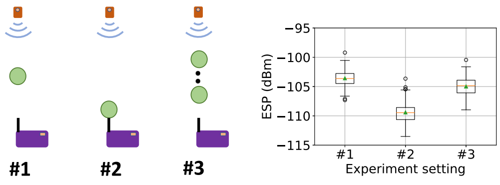

(a) Experimental Settings (b) ESP for three settings

Fig. 6. The diffracted signal strength.

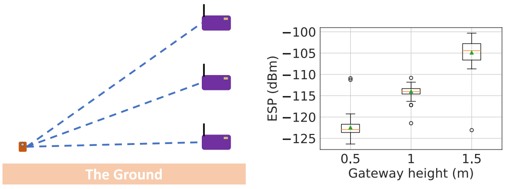

(a) Experimental Settings (b) ESP for three settings

Fig. 7. The effect of ground absorption.

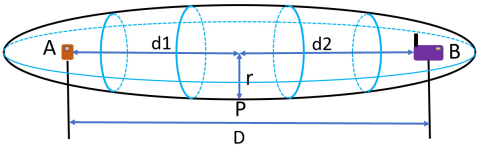

Fig. 8. The illustration of FFZ.

All of these validations demonstrate that the link quality can be influenced by the surrounding objects, and the “path” cannot be considered as simply the visual LoS path between the sender and receiver. Instead, more attention should be given to the surrounding regions along the visual LoS path when estimating path loss. To address this issue, we propose the adoption of FFZ in path loss calculations, as it takes into account the surrounding environment.

4.2 First Fresnel Zone for LoRa Signal

The FFZ refers to the 3D ellipsoid region around the direct path through which the received signal passes. Figure 8 depicts that a point P lies on the surface of the FFZ if and only if

$$\sqrt{d_1^2 + r^2} + \sqrt{d_2^2 + r^2} = (d_1 + d_2) + \frac{\lambda}{2}, \tag{5}$$

where λ refers to the wavelength. This equation quantifies confocal prolate ellipsoidal-shaped regions with the sender and receiver located at two focal points. This theory suggests that all media within the FFZ shadows the signal, not just media along the direct path.

Based on Equation (5), the volume of the FFZ increases proportionally with wavelength. For instance, at a distance of 100 m, the maximum radius of the FFZ could be 2.8 m. This highlights the need to quantify the shadowing of the surrounding area over the direct path.

4.3 Design of *FLog*

This section provides the design details, including the overview, portion quantification, intrinsic PLE fitting, and parameter adaptation mechanism.

4.3.1 Overview. Except for the foliage and free space, we also need to consider the ground shadowing effect. Because the FFZ of the LoRa signal has intersections with the ground due to the low height of sensor nodes. Therefore, we update the final PLE calculation Equation (4) as follows:

$$PLE_{comb} = P_{open} \cdot \alpha + P_{foliage} \cdot \beta + P_{ground} \cdot \gamma, \tag{6}$$

where two new variables, P_{ground} and γ, are introduced to represent the ground shadowing effect. The values of α, β, and γ correspond to the intrinsic PLEs when the wireless signal propagates through free space, foliage, and ground, respectively. The portion of free space, foliage, and

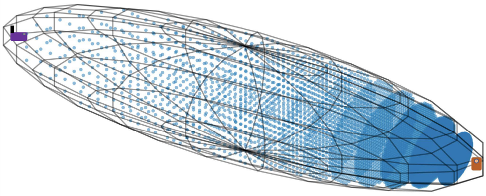

Fig. 9. The illustration of sampling.

Table 2. Average Sampling Results at 60 m vs. *p_gap*

p_gap (m)	0.25	0.3	0.35	0.5	1.0
P_{open}	0.686	0.686	0.687	0.690	0.702
$P_{foliage}$	0.313	0.313	0.312	0.309	0.297

ground in the FFZ is denoted by P_{open}, $P_{foliage}$, and P_{ground}, respectively. The final PLE_{comb} in the FFZ is obtained as a weighted combination of α, β, and γ, where the corresponding weights are P_{open}, $P_{foliage}$, and P_{ground}. In an orchard, all the pairs of senders and receivers share the same α, β, and γ, but have different final PLE_{comb} due to the varying weights. The next two subsections explain how to determine their values.

4.3.2 Portion Quantification. The weights of each media in an FFZ are calculated by computing the volume of each media and dividing it by the total volume of the FFZ. However, computing this volume requires solving a triple integral in a constrained 3D space, which is computationally intensive and time-consuming. In this article, as shown in Figure 9, we used a sampling approach by dividing the FFZ into multiple planes with equal spacing. Each plane was then further sampled into numerous points.

Specifically, we incremented the number of corresponding media points by one if a sampling point was located within that media. For example, if a sampling point was in free space, then we incremented the free space points by one. The portion of each media was then calculated by dividing the number of points contained in that media by the total number of points in the FFZ. Therefore, the sum of the portions for all three media types should be one.

Sampling Planes: The first sampling plane is located at $d_0 = 1\ m$, which is the reference distance in the Log-Normal Shadowing model. The remaining sampling planes are equally spaced at an interval of *p_gap*. We change the value of *p_gap* from 0.15 to 0.35 m to calculate the portions of different mediums. Table 2 shows that there is no significant impact on sampling results for different *p_gap* values less than 0.5 m. Considering the computational burden and sampling effectiveness, we empirically set $p\_gap = 0.25\ m$.

The number of sampling points in each plane varies and is proportional to the signal energy in the plane, which is calculated by multiplying the power flux density by the area of the plane. The radius of the plane can be determined via Equation (5). The power flux density of a sampling plane decreases proportionally to the square of the distance [46], i.e., $4\pi d^2$, indicating that the number of sampling points in each plane should similarly decrease with distance. Therefore, the total number of sampling points on a plane i is given by $N^i_{plane} = N_{ref} \cdot S_i \ / \ 4\pi d_i^2$, where N_{ref} is a constant that can be adjusted to control the total number of sampling points, S_i is the area of plane i, and d_i is the distance between the sender and the plane i. Table 3 indicates that N_{ref} has no impact on sampling results if the sampling points are adequate. We set N_{ref} as 590 k in the experiments.

Table 3. Average Sampling Results at 60 m vs. N_{ref}

N_{ref}	2360 k	590 k	148 k	74 k	18 k
P_{open}	0.686	0.686	0.686	0.686	0.687
$P_{foliage}$	0.313	0.313	0.313	0.313	0.313

Table 4. Comparison of the Sampling Point Numbers for Trees of the Same Shape and Distance to the Sensor Node, But in Different Areas of the FFZ

	#Sampling points in canopy	#Sampling points in trunk
A tree in the middle of FFZ	73,076	1,568
A tree at the edge area of FFZ	5,692	129

Sampling Points in a Plane: Due to diffraction loss, the power flux density of the received signal is higher along the major axis than at the edge of the FFZ [41, 72]. Accordingly, we prioritize sampling at the circle center over sampling at the edge. Specifically, we first determine the number of sampling circles within this plane and then progressively increase their radii quadratically from the center to the edge.

In this way, the sampling points are denser when closer to the major axis, as shown in Figure 9. Table 4 provides an example of two trees with the same shape and distance to the sensor nodes, but triggering substantially different numbers of sampling points, reflecting the rationale that trees along the major axis should be prioritized due to higher power flux density.

4.3.3 *Intrinsic PLE Fitting.* To calculate the final PLE_{comb} in Equation (6), we also need to determine the values of α, β, and γ. The process for obtaining these values is outlined below.

To determine the value of γ, we utilized non-foliage data from Figure 7 and applied the least square algorithm to Equation (6), where $P_{foliage} = 0$ and $\alpha = 2$. This yielded a value of $\gamma = 5.39$. The ground's dynamic nature poses challenges to algorithmic stability due to its high PLE, which significantly affects signal strength. Incorporating its variability can skew PLE values for air and trees, potentially impeding algorithm convergence. To maintain stability, we keep the ground's PLE constant and adjust the PLEs of air and trees to offset any ground variations. Hence, the 5.39 will serve as the default for the remainder of the article unless otherwise noted.

To determine the values of parameters α and β, we collected packets at multiple pairs of transceivers in our testbed, as described in Section 5.1.4. For each pair, we calculated three portions: P_{open}, $P_{foliage}$, and P_{ground}. We then combined Equations (1)–(3) to obtain the final PLE_{comb}, using the RSSI and SNR values obtained after receiving a packet. Thus, the only unknown variables in Equation (6) are α and β. We then employed a least square error fitting algorithm to determine the optimal values of α and β.

4.3.4 *Parameter Adaptation Mechanism.* For long-term maintenance, the estimation needs to be adapted to ensure continuously high accuracy. Specifically, the parameters in Equation (6) could be impacted by different environmental dynamics, which can be categorized into four scenarios:

(1) Short-term environmental noise variation.
(2) *Transient weather changes*, e.g., temperature.
(3) *Foliage density changes* on a yearly cycle due to the growth and loss of leaves and fruits.
(4) *Long-term foliage shape changes:* Shape changes as trunk and branch grow over years.

To mitigate the impact of dynamic (1), we collect multiple packets to compute the average signal power as the reference signal power at a given location. Environmental dynamics (2) and (3) can affect α and β in Equation (6). To recalibrate these two parameters, we use the most recently

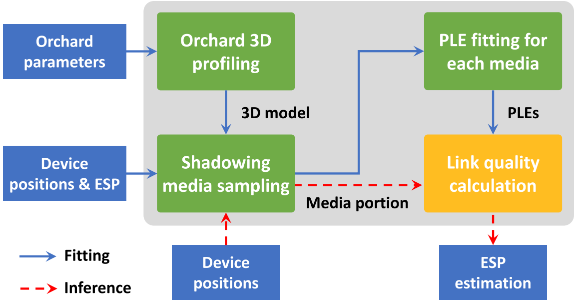

Fig. 10. Workflow of the *FLog*, where the term *device* refers to both the LoRa node and the gateway.

received N packets from all sensor nodes. When a new packet is received, we obtain its measured ESP. Thus, the ESP of the past $N \times M$ packets from M nodes will form $N \times M$ equations to recalibrate α and β, as shown in the example equations below (where $i = 1, 2, \ldots, N$ and $j = 1, 2, \ldots, M$):

$$\begin{bmatrix} PLE_1^1 \\ \vdots \\ PLE_j^i \\ \vdots \\ PLE_M^N \end{bmatrix} = \begin{bmatrix} P_{\text{open}_1} & P_{\text{foliage}_1} & P_{\text{ground}_1} \\ \vdots & \vdots & \vdots \\ P_{\text{open}_j} & P_{\text{foliage}_j} & P_{\text{ground}_j} \\ \vdots & \vdots & \vdots \\ P_{\text{open}_M} & P_{\text{foliage}_M} & P_{\text{ground}_M} \end{bmatrix} \begin{bmatrix} \alpha \\ \beta \\ \gamma \end{bmatrix} \tag{7}$$

The new α and β could be fitted by employing the non-linear least square algorithm on the set of equations shown above. We empirically set $N = 5$. Note that all links in an orchard at the same cycle share the same α, and β.

The dynamic (4) refers to changes in the 3D profile of the orchard, which affect P_{open} and $P_{foliage}$ in Equation (6) for all nodes but not α and β. To handle this dynamic, it is necessary to remeasure the tree height, trunk height, and canopy width to rebuild the 3D profiles. This is expected to be done every year or even longer.

4.4 Workflow of *FLog*

Figure 10 summarizes how *FLog* works, including all modules mentioned in the previous section and their input and output. The farmer provides input parameters for generating the 3D orchard, and *FLog* estimates the link quality between any two locations in the orchard based on these parameters. The user can choose a configuration that they think is best suited for their orchard. Specifically, *FLog* requires the following parameters from the farmer: tree profile, layout, and deployment parameters.

(1) Tree Parameters: Tree height, trunk height, and canopy width: They are used to build the 3D profile of a single tree. As the growth accumulates, the user may measure these parameters every year or longer.
(2) Layout Parameters: The distances between adjacent rows and adjacent trees in one row are required for the layout configuration. These factors will never change. There might be several blank positions for removed dead trees. *FLog* also accepts such input or updates.
(3) Sensor and gateway position (optional): If the application requirements dictate the placement of the sensor and gateway, then the user should input their designated positions. Or we can determine the optimal position based on *FLog*.

Using the parameters above, *FLog* creates an FFZ between any two locations. It then calculates the portion of foliage, free space, and the ground within this zone and estimates the link quality via Equations (2), (3), and (6). Additionally, *FLog* utilizes a parameter resetting mechanism to tune our model's parameters, which adapts to different environmental dynamics.

We made the assumption that all trees share the same shape. While this generalization might seem oversimplified, it is a necessary approach considering the impracticality of measuring every individual tree's shape. To account for this simplification, we fit each medium's PLE to ensure our model aligns well with the measured signal strength. This helps mitigate the potential impact of our tree shape simplification on system performance.

4.5 Applications of *FLog*

FLog can be used to deploy LoRa networks in orchards, e.g., determining gateway coverage, sensor placement, and network resource allocation. We use gateway coverage as an example to demonstrate the application of *FLog*.

4.5.1 Gateway Coverage Estimation Application. Our path loss model can estimate gateway coverage by determining if a gateway can cover a specific location. Specifically, if the PDR exceeds 80%, then a gateway could cover a given location [74, 76]. Thus, our path loss model can estimate the PDR prior to deploying LoRa networks.

Packet Devilry Ratio: PDR can be estimated by the BER and packet size, which is calculated as follows [44]:

$$PDR = (1 - BER)^{8 \cdot S_p}\ , \tag{8}$$

where S_p is the packet size in bytes, e.g., 8 bytes in our implementation; the BER is calculated by Equation (9).

BER Calculation: LoRa links are exposed to environmental noise (e.g., additive white Gaussian noise) and other types of noises. The quality of LoRa links can be quantified by SNR. Once SNR and SF are determined, we can calculate BER using Equation (9) [20]:

$$BER \approx 0.5 \cdot Q\left(\frac{\sqrt{\mathrm{SNR} \cdot (\mathrm{M}+1)} - \left((H_M)^2 - \frac{\pi^2}{12} \right)^{1/4}}{\sqrt{H_M - \sqrt{(H_M)^2 - \frac{\pi^2}{12}} + 0.5}} \right), \tag{9}$$

where $M = 2^{SF} - 1$, $H_M = \sum_{k=1}^{M} \frac{1}{k}$ denotes the Mth harmonic number. $Q(x) = \frac{1}{\sqrt{2\pi}} \cdot \int_x^\infty \exp(-\frac{y^2}{2})dy$ is the Q-function, i.e., the tail function of the standard normal distribution. Considering that LoRa is the orthogonal signaling, 0.5 before the Q-function means that for a symbol error, only half of the bits in the symbol could be in error [44]. The Q-function part models the probability that the magnitude of noise envelopes is larger than the magnitude of LoRa signals of interest envelopes, which are modeled as Rayleigh distribution and Rician distribution, respectively.

Signal-to-Noise Ratio: In Equation (1), we can obtain the SNR as long as the ESP and RSSI is known. Fortunately, given any node and gateway location, the ESP could be predicted by our path loss model. We obtain the received RSSI by averaging the all collected data. By this way, we can compute the expected SNR as follows:

$$\mathrm{SNR} = 10 \cdot \log_{10} \frac{1}{10^{\frac{\mathrm{RSSI} - \mathrm{ESP}}{10}} - 1}. \tag{10}$$

In Section 5.4, we will compare the predicted gateway coverage by using three path loss models.

4.5.2 Benefits for Farmers. We will use the example of gateway coverage estimation to analyze the benefits for farmers offered by *FLog*. If the estimated propagation path loss is greater than the actual value, then more gateways will be required than necessary, leading to an increase in gateway building costs. Conversely, if the estimated path loss is less than the actual value, then some nodes may not be able to connect with gateways, rendering the sensor network incomplete and unsuitable for practical applications. Thus, an inaccurate propagation model can significantly impact the efficiency and effectiveness of the sensor network. In Section 5.4, we quantify the benefits using real measurements in a specific orchard.

4.5.3 Obstacles with Non-uniform Geo-distributions and Shapes. For missing trees that are cut down due to illness, we can easily delete the tree from the 3D modeling by inputting the index. For forests where trees are irregularly placed and differ in species, age, and shape, surveying and mapping would be labor intensive. In these cases, we can use satellite images and radars to estimate the shapes of trees [15]. For urban areas, buildings are constructed using different materials and have varying PLEs. Additionally, large smooth surfaces create mirroring reflections, resulting in reflection-based multipath being the major component, which is different from the orchards. We suggest using NeRF-based solutions for urban cases [77].

4.5.4 Reverse Uses for Wireless Media Sensing. Given that changes in PLE are primarily driven by variations in foliage density, *FLog* can also be used inversely to estimate orchard biomass. Specifically, it can assess leaf health in the spring and fruit mass during the summer and fall [5]. This approach offers the advantage of wide-area sensing without the need for specialized hardware. However, achieving reliable results requires larger datasets spanning various tree ages and hundreds of orchards to facilitate robust, controlled comparisons. We leave this exploration for future work when *FLog* is widely adopted.

5 Evaluation

We evaluate the overall performance of *FLog* in Section 5.2, Then, we study the performance under different factors in Section 5.3, followed by the performance on the application study in Section 5.4.

5.1 Experiment Setting

5.1.1 Hardware Implementation. Figure 11 depicts the used hardware of LoRa node and gateway. LoRa nodes are handcrafted with SX1276 Radio [2] on the Arduino Uno host boards [3]. They are equipped with a 3,000-mAh power bank. They work in the frequency band 904.3 MHz. The RAK831 Pilot Gateway [56] is used as the LoRa receiver to receive LoRa packets. It consists of a Raspberry-Pi 3, an RAK831 LoRa Concentrator and a converter board with GPS for routing the signals between the Raspberry and the RAK831. Both nodes and gateways are using omni-directional antennas, with antenna gains of 5 and 3 dBi, respectively. The gateway executes a thread of LoRa Packet Logger [1] that demodulates packets and stores them as comma-separated values files. Our model is implemented with Python script on a PC server with an Intel Core i9-11900KF @ 3.50 GHz CPU with 16 cores. The packet reception information on the gateways are aggregated in the cloud server with Kubernetes and auto-configuration [32, 66].

5.1.2 Benchmarks. We compare the performance of *FLog* with the following multiple baselines.

- *Log-Normal Shadowing Model [46]:* It is calculated by Equation (3). We use the collected data to fit PLE in the orchard scenario. It is referred to as "Log."
- *Line-based Log-Normal Shadowing Model:* It is our strawman solution, which is introduced in Section 3. We call it "LLog."
- *Empirical Foliage Loss Models:* They include Weissberger [62], **ITU Recommendation (ITU-R)** [45], COST235 [27], Two-ray ground-reflection model [78] and Okumura-Hata

(a) LoRa node (b) LoRa gateway

Fig. 11. The hardware implementation.

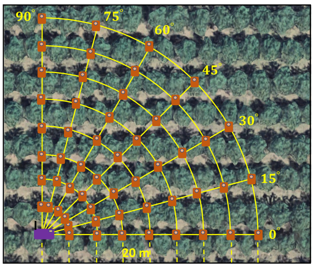

Fig. 12. The testbed layout in an almond orchard.

models [16]. All these models that are parameterized or have multiple variants have been carefully evaluated and reported as their best performance.

5.1.3 Performance Criteria. The estimation accuracy is quantified by errors between the predicted ESP and the corresponding actual value for each packet. The unit of errors is decibel-milliwatts,

$$\text{ESP error} = (y_i - \hat{y}_i)\,, \tag{11}$$

where y_i is the measured ESP for the ith received packet and $\hat{y}_i$ is the predicted ESP value.

5.1.4 Experiments in an Almond Orchard. We chose almond orchards as the main focus of our evaluation, since they are a critical agriculture industry in the US. In 2021, the US produced 2.5 billion pounds of almonds, with a value of over 7 billion dollars [59]. Moreover, the estimated almond acreage in California was 1.64 million acres, making it the largest producer of almonds in the world [59]. We also tested *FLog* in a walnut orchard, which is another dominant arbor crop.

Figure 12 shows locations of LoRa nodes and a gateway in an almond orchard with a size of 200 × 200 m^2. In this orchard, trees are planted in a line with 4.88 m distances, and lines are separated by 6.66 m. The almond trees are 6.1 m in height and 2.8 m in width. The heights of the LoRa node and the gateway are set as 0.45 and 10 m. The transmission power is 14 dBm, SF is 10, bandwidth is 125 kHz, and coding rate is 4/5. We collect packets from the spatial and temporal dimensions to evaluate our model.

We do not rely on the GPS to determine the physical locations of LoRa nodes, due to its large localization error in orchards [50, 68]. Instead, we take advantage of the uniform arrangement of trees in orchards. Trees are consistently spaced both along the rows and across columns. By counting the number of trees, we can accurately compute the distance between any two positions. Specifically, we use a 3D Cartesian coordinate system to represent these positions: the x- and y-axes correspond to the directions along and across the orchard rows, respectively, while the z-axis points upwards. The origin of this system is aligned with the gateway's position on the ground. We determine the distance between any nodes and the gateway using the Euclidean distance formula.

5.1.5 Datasets. We measure the received packets at a large number of locations in an orchard. We also conduct experiments at some locations for months.

Spatial Dimension Dataset: As shown in Figure 12, the gateway is located in the lower-left corner of one of the 90° fan-shaped areas of the orchard. We have deployed LoRa nodes at 56 locations across this fan-shaped area to collect packets. For each received packet, we calculate the ESP by using its RSSI and SNR. The nodes are placed at communication distances ranging from 20 to 160 m, with a step size of 20 m. We measured seven directions ranging from 0° to 90°, with a step size of 15°. At each location, the nodes transmit an 8-byte packet to the gateway every 1.5 s for a duration of 1.5 min. The experiment was conducted for a duration of 10 hours in

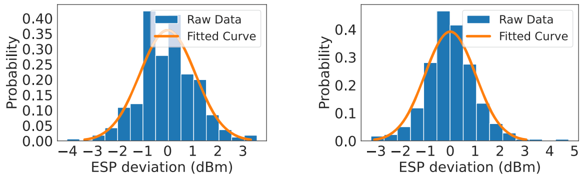

(a) Environmental noise (60 m) (b) Environmental noise (100 m)

Fig. 13. The ESP deviation distribution for two different communication distances.

the autumn of 2,022, and 2,900 packets were collected in total. The ESP ranges from −125 to −85 dBm, corresponding to an SNR range of $[-15, 7]$ dB. The collected data is unavoidably affected by the environmental noise at each location. We compute the average ESP at each location as the reference ESP. The ESP deviation is obtained by comparing the average ESP and the collected ESP of each packet. Figure 13 shows that the ESP deviation at two distances generally follows a Gaussian distribution with a deviation of 1.1 and 1.0 dBm.

Given the consistent planting patterns, we deduce that patterns, signal strengths, and propagation characteristics observed in one quadrant will reflect those in the remaining three. Consequently, by strategically positioning our gateway in a corner, we can capture representative data without the need for exhaustive measurements across the entire orchard.

Temporal Dimension Dataset: We collected another dataset that covers four environmental dynamics, as described in Section 4.3.4. Four LoRa nodes are deployed at four locations randomly selected from Figure 12 to collect long-term data over a period of 4 weeks in the spring (January and February 2023). The transmission settings used for collecting the data are the same as those used for the spatial dimension data. We collected data continuously for 24 hours each week, resulting in a dataset of 69,173 packets. The dataset contains three environmental dynamics: (1) Short-term environment variations. (2) Transient weather changes, including temperatures ranging from 26.2 to 65.5°F and precipitation ranging from 0 to 0.15 inch/hour. (3) Foliage density changes. In the final week of the 4-week period, almond trees started to bloom with flowers. By combining this with the spatial dimension data, foliage density can be classified into three categories: trees with dense leaves, trees without leaves, and trees with flowers.

Finally, dynamic (4), the long-term foliage shape changing, was emulated by collecting data in another almond orchard, where the almond trees have a height of 4.5 m and width of 2.6 m, which corresponds to changing trunks and branches, compared to the almond trees shown in Figure 12.

Fitting and Testing Data: In the spatial dimension of the data, we used measurements collected from four randomly selected distances to fit the parameters in our path loss models, such as α and β. These measurements are referred to as fitting data. The data from the remaining four communication distances were used as testing data. To obtain the optimal parameter values on the fitting data, we employed the least square approximation method. These parameter values were then used to estimate the ESP on the testing dataset.

5.2 Overall Performance

We evaluated the performance of all modes on both spatial and temporal dimension data. To measure the impact of different distances on estimation error, we combined all directions' data at one distance. For a specific distance, we studied the performance of all models in different directions with an interval of 15°.

5.2.1 Spatial Dimension. In the fitting and testing data, four communication distances were randomly selected from eight distances in our testbed. Therefore, there are $\binom{8}{4} = 70$ combinations

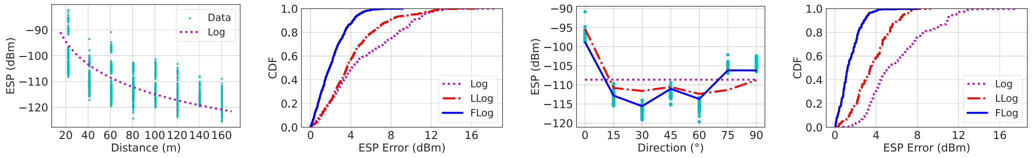

(a) ESP *vs.* distance (b) Distances and directions (c) ESP *vs.* direction (60 m) (d) All directions at 60 m

Fig. 14. The overall performance of three models for different communication distances and directions. Figure (a) does not draw the fitted curve of the LLog and *FLog*, it is because they have different estimated values at different directions for one communication distance. Panel (c) plots the estimated value in different directions when the horizontal distance between LoRa nodes and the gateway is 60 m. The curve of the Log model is a horizontal line, which could not handle the direction.

to select the fitting and testing data. For each set of fitting data, we obtained corresponding fitted values of α and β. After analyzing all 70 combinations, we found that the mean value of α was 1.98 with a standard deviation of 0.11, while the mean value of β was 5.07 with a standard deviation of 0.17. This result provides the interpretable clues for the shadowing feature of media. We report all the estimation errors for these 70 combinations in Figure 14(b).

Communication Distance: Figure 14(a) presents the estimated curves of Log with changing communication distances. We do not draw the curve of the LLog and *FLog*, because they have different estimated values in different directions for a given distance, while the Log model has one average value for each distance. We can observe a trend wherein the measured ESP correlates linearly with the logarithm of the distance. Figure 14(b) quantifies the estimation error for different models in the CDF curve (cumulative distribution function). The average error of *FLog* is only 2.85 dBm, showing great performance improvement over other models in terms of link quality estimation. In particular, *FLog* decreases the ESP estimation error of Log and LLog by 42.7% and 35.2%, respectively. This is because Log does not consider the influence of direction on the received signal power and can only estimate the signal power based on the communication distance in Equation (3).

Although LLog is aware of the ESP variation in different directions, it only considers the obstacle of lines between the node and gateway. However, the signal is concentrated in the FFZ based on the diffraction theory [46] and our preliminary experiments in Section 4. Therefore, *FLog* developed a more reasonable model to consider the shadowing effects in the FFZ.

Direction: Figure 14(c) and (d) present the fitted curves of all models and the estimation errors with different directions at a horizontal distance of 60 m. It is observed that Log is unaware of directions and thus provides a horizontal line as the estimated curve, which remains unchanged for different directions. Although LLog considers the influence of direction, it produces unstable performance. At direction 75°, LLog produces the largest error, that is, 5.93 dBm. This is due to the fact that LLog considers only the shadowing in the line of the propagation path, which results in overestimating or underestimating the ESP of the received signal.

Empirical Foliage Loss Models: Table 5 presents the average estimation ESP error on the test data for five different foliage loss models. These foliage models provide worse prediction accuracy compared with the Log, LLog, and *FLog* models. There are three reasons for the poor performance.

First, these models are developed using different frequency channels and have different attenuation in the same situation, since the wavelength is different. Thus, the empirical models cannot be directly applied to our scenarios. Second, these loss models have no adjustable parameters to adapt to different scenarios. However, the Log-Normal Shadowing model can adapt to various situations by fitting its parameters, such as PLE. Hence, it can perform well if we fit it with the collected data

Table 5. The ESP Estimation Error for Other Models

Models	Weis.	ITU-R	COST235	O-H	Two-ray
ESP Error (dBm)	41.6	111.2	87.4	12.7	72.3

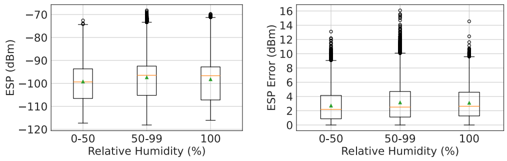

(a) ESP *vs.* humidity (b) ESP error *vs.* humidity

Fig. 15. Impact of the dynamic (2): humidity.

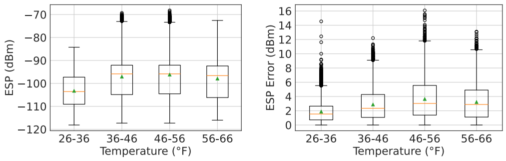

(a) ESP *vs.* temperature (b) ESP error *vs.* temperature

Fig. 16. Impact of the dynamic (2): temperature.

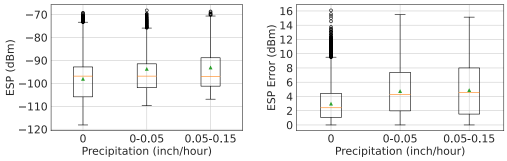

(a) ESP *vs.* precipitation (b) ESP error *vs.* precipitation

Fig. 17. Impact of the dynamic (2): precipitation.

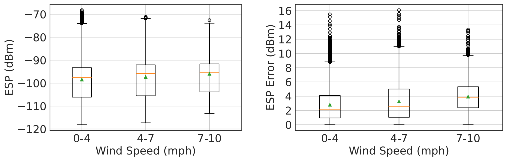

(a) ESP *vs.* wind speed (b) ESP error *vs.* wind speed

Fig. 18. Impact of the dynamic (2): wind speed.

on the specific case, compared with those path loss models with fixed parameters. Third, those models cannot handle the ESP deviation in different directions. This is similar to the Log-Normal Shadowing model. They can only consider the effect of the communication distance on the signal strength but not on other factors such as directions.

5.2.2 Temporal Dimension. We use temporal dimension data to test the models' performance on the three different environmental dynamics. We apply our parameter resetting mechanism to all path loss models, which uses the most recently received packets to calibrate models' parameters. Note that the environmental dynamic (1) was addressed by averaging the received ESP of multiple packets.

Environmental Dynamic (2) - Transient Weather Changes: We first obtain the temperature, precipitation, wind speed, and humidity from a weather station [52]. Next, we group the data based on the value range of corresponding weather factors at the time of collection. Figures 15–18 illustrate the ESP values and ESP estimation error of *FLog* under different weather conditions.

Figure 16 depicts that ESP at 36°C and 66°C is higher than that at 26°C and 36°C. Figure 17 shows the discrepancy in different precipitation levels. They are caused by waterproof cover deformation. There is no explicit difference if the data trace of that node (the blue line in Figure 28) is removed.

As shown in these four figures, models achieve no increased ESP prediction error for different temperatures, humidity, wind speed, and precipitation levels. *FLog* always outperforms Log and LLog in any weather condition groups, with an average improvement of 39.8% and 41.5%, respectively. This indicates the effectiveness of our parameter resetting mechanism in adapting to dynamic (2). It is reasonable, because the proposed mechanism can adjust the values of parameters α and β based on the recently received packets. We analyzed the received ESP of LoRa signals under different temperature and precipitation conditions. Our findings indicated that the difference in signal power at different temperatures or precipitations was small. This small difference may

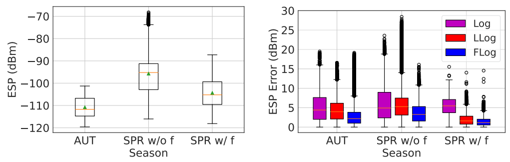

(a) ESP *vs.* season (b) ESP error *vs.* season

Fig. 19. Impact of the dynamic (3): foliage density.

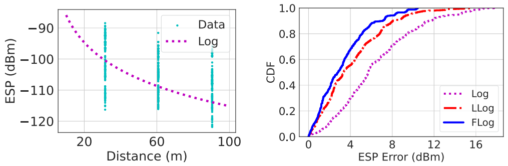

(a) ESP *vs.* distance (b) ESP error distribution

Fig. 20. Impact of the dynamic (4): foliage shape.

be attributed to the effects of atmospheric and vapor molecules on electromagnetic waves, which become more apparent at frequencies exceeding 10 GHz. However, the absorbance for 900 MHz bands at short distances ($\leq$50 km) is negligible [36, 38].

Environmental Dynamic (3) - Foliage Density Changes: In the spatial and temporal dimension dataset, foliage density has three statuses: trees with dense leaves, trees without leaves, and trees with flowers, which are referred to as "AUT," "SPR w/o f," and "SPR w/ f," respectively. We use our proposed parameter resetting mechanism to adapt to this dynamic. Figure 19 illustrates the received signal power and ESP estimation error for the three foliage density statuses. Figure 19(a) indicates that foliage density significantly impacts the received signal power. *FLog* handles foliage density variations by continuous parameter refitting scheme. In particular, Figure 19(b) shows that *FLog* is capable of adapting well to this dynamic, with estimation errors of 2.85, 3.61, and 1.42 dBm across three foliage density states.

Environmental Dynamics (4) - Long-Term Foliage Shape Changes: We collected data in another almond orchard to evaluate the impact of growing stages on our proposed method, which we refer to as environmental dynamic (4). The transmission settings of the nodes were the same as those used in the testbed, and we collected data at three communication distances with seven different directions (0°, 15°, 30°, 45°, 60°, 75°, and 90°). We used the parameters fitted from the testbed data to estimate the link quality in the new orchard. To reconstruct the 3D structure, *FLog* requires measuring one tree, as described in Section 4.4. The new 3D structure will be used to calculate P_{open}, $P_{foliage}$ in Equation (6).

The results, shown in Figure 20, indicate that *FLog* achieved an average estimation error that was reduced by 48.3% and 16.2%, compared to Log and LLog, respectively. Figure 20(a) shows that the Log model could roughly fit the measured signal over the communication distance. However, *FLog*'s performance was comparable to the overall performance reported in Section 5.2, with an average ESP of 2.51 dBm compared to 3.42 dBm for Log. This confirms that *FLog* is insensitive to different almond fields and growing conditions.

Figure 20(b) illustrates that LLog achieved a similar ESP error to *FLog*. This could be attributed to the smaller shape of trees in this orchard, and LLog generates a smaller shadowing media portion, closer to that of *FLog*. The statistics indicate that the two methods had comparable estimations of $P_{foliage}$, averaging 0.17 and 0.24. Hence, LLog delivers a performance comparable to *FLog*.

5.3 Generalizability Study

To evaluate the generalizability under various experimental settings, we collect wider datasets under different orchard species, different gateway heights, and sensor heights.

5.3.1 Impact of Orchard Species. Different orchard types can introduce varying shadowing effects, making it logical to expect distinct β values for each species. Recognizing the distinct foliage shape and density differences between walnut and almond trees, we selected the walnut orchard to ascertain the adaptability of *FLog* in such varied settings.

Fig. 21. The illustration of the almonds and walnuts of the experiments.

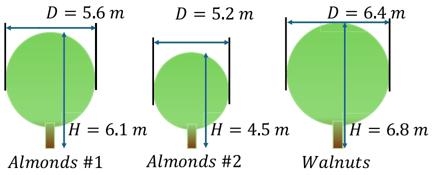

Fig. 22. The shape comparison between walnuts and almonds in the experiments.

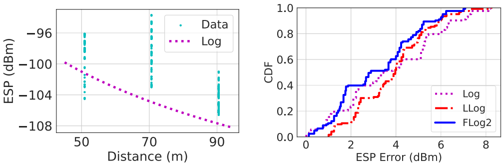

(a) ESP *vs.* distance (b) ESP error distribution

Fig. 23. The impact of the orchard species.

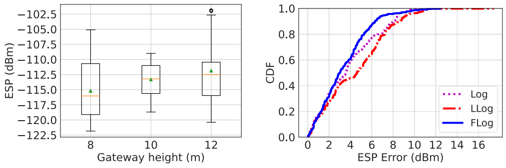

(a) ESP *vs.* height (b) ESP error distribution

Fig. 24. The impact of the gateway height.

To fit parameters in a walnut orchard, we collected data at a horizontal distance of 50 m and 90 m in three directions (30°, 60°, and 90°). We then utilized three path loss models with newly fitted parameters to estimate the ESP in the same walnut orchard, the evaluation is conducted on the data collected at 70 m in three different directions (30°, 60°, and 90°). All other transmission settings remained the same as the testbed.

As shown in Figure 23(a), similar trends were observed in the walnut orchard as in the almond orchard, i.e., the ESP of the received signal decreased with increasing communication distance. Figure 23(b) reports the CDF of the ESP estimation error for different models, which shows that *FLog* provides the highest estimation accuracy. The *FLog* reduced the error by 15.4% and 18.0% for the Log and LLog models, respectively. The illustration of the orchards and tree shapes are in Figures 21 and 22.

5.3.2 Impact of Gateway Height.

We investigated the effect of gateway height on performance gain by conducting experiments at varying heights. The maximum height of our tripod was 12 m, and we set the gateway height at 8, 10, and 12 m, with a fixed horizontal distance of 80 m between the sensor and the gateway. We collected data in four different directions at each gateway height (0°, 30°, 60°, and 90°).

The results, shown in Figure 24(a), demonstrate that the ESP of the received signal increases as the gateway height increases from 8 to 12 m, which matches the expectation. Figure 24(b) shows that *FLog* could fit the measured ESP well at all gateway heights, compared to the other two methods. Besides, LLog performed worse than Log, because $P_{foliage}$ in LLog overreact to the change of gateway height, e.g., $P_{foliage}$ was incorrectly estimated at an average of 0.541. Therefore, LLog performed worse than the other two models.

5.3.3 Impact of Sensor Height.

We also investigated the effect of sensor height on performance gain. Placing the sensor on the ground can significantly affect signal propagation, so we varied the sensor height to observe the impact. We tested heights of 0.15, 0.45, and 1.2 m, with a fixed horizontal distance of 80 m between the sensor and the gateway. Each height corresponds to a classical deployment position of sensors: on the ground, tied on the trunk, and hanged on the branches. We collected data in four directions at each sensor height, i.e., 0°, 30°, 60°, and 90°.

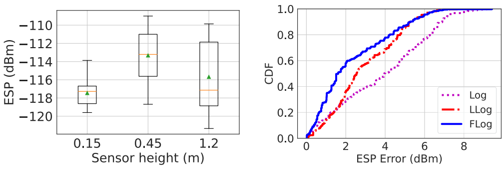

(a) ESP *vs.* height (b) ESP error distribution

Fig. 25. The impact of the sensor height.

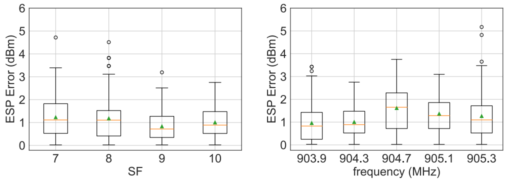

(a) ESP error *vs.* SF (b) ESP error *vs.* frequency

Fig. 26. Impact of the transmission parameters.

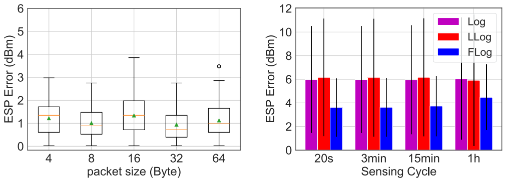

Fig. 27. Impact of packet size and sensing cycle.

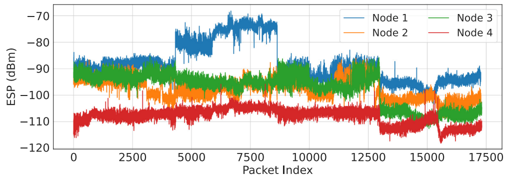

Fig. 28. The received signal power at four nodes over a period of 4 weeks.

Figure 25(a) shows that increasing the sensor height from 0.15 to 0.45 m improved the received signal's ESP. However, the signal strength decreased when the sensor height was 1.2 m, likely due to the almond tree's leaves blocking the signals at the LoRa nodes. Therefore, we set the sensor height to 0.45 m. Figure 25(b) displays the estimated ESP error for the three methods, with *FLog* performing the best compared to Log and LLog models. Notably, *FLog* reduced the average ESP error by 27.1% and 12.0%, respectively. The experiment also suggests that tying the sensor node to the trunk is the best option.

5.3.4 Impact of Transmission Parameters. We conducted experiments to study the effects of various parameters on our model. Theoretically, transmission power, antenna gain, frequency, and SF do not have a direct impact on the path loss exponent, which is what the link quality models aim to estimate. The packet size may slightly affect the calculation of SNR on the hardware and thus lead to a variation in ESP. Figures 26 and 27(a) show the estimation error for different SFs, frequency bands, and packet sizes, and the results demonstrate that none of these parameters have a significant effect on the ESP.

5.3.5 Impact of Sensing Cycle. We utilize the most recently received N packets to perform the parameter resetting mechanism, where N is set to 5. The performance of this mechanism may be influenced by the sensing cycle, which is the time between two adjacent transmitted packets. In our testbed, each node sends 45 packets every 15 min with a 20-s interval. To simulate a 15-minute sensing cycle, we use the 1st, 46th, 91st, 136th, and 181st packets to recalibrate our model's parameters, which are then used to predict the link quality of the 226th packet. This allows us to employ our parameter resetting mechanism at different sensing cycles. Figure 27(b) shows the error bars with different sensing cycles for three models, depicting the standard deviation from the average. We can find that the duration of the sensing cycle has a minimal impact on the performance of our model. Specifically, compared to a sensing cycle of 20 s, the estimation errors of *FLog* increase by 0.87%, 4.03%, and 9.56% with sensing cycles of 3 min, 15 min, and 1 hour. Figure 28 illustrates the received signal power over a period of 4 weeks. It can be observed that the link quality at a particular location in the orchards remains relatively consistent, indicating that changing the sensing cycle has minimal impact on the estimation error.

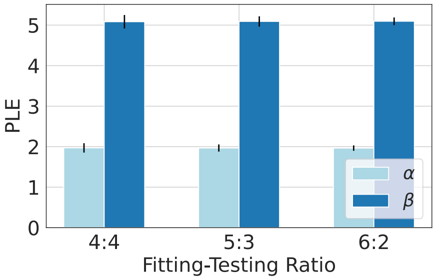

Fig. 29. The values of parameter of α and β under different ratios of the fitting and testing data.

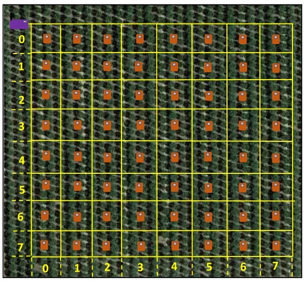

Fig. 30. Illustration of collecting data in a new almond orchard for gateway coverage estimation.

It should be noted that for node #1, there were two significant changes in ESP at packet indexes 4,316 and 8,633, respectively. The first change occurred due to a gusty wind that caused the waterproof cover behind the antenna to lift up like a reflection mirror, resulting in a significant increase in ESP. The cover was manually recovered at the second change point, which caused the ESP to return to normal levels. Although this incident caused an increase in errors, its impact on the comparison between different sensing cycles is negligible. This is because two outliers would only affect five estimations in our parameter resetting mechanism. Second, during the last week of the 4-week period, almond trees began to bloom with flowers, resulting in a significant decrease in the received LoRa signal power for all four nodes.

5.3.6 Impact of Ratio between Fitting and Testing Dataset. In the previous sections, the default ratio is 4:4. We evaluated our model with ratios of 5:3 and 6:2. The settings of 5:3 and 6:2 had a similar performance to the ratio of 4:4, with a negligible difference in average estimation error of 0.09 and 0.04 dBm. We also reported the obtained values of the α and β in Figure 29. The error bar represents one standard deviation from the average. We find that the fitted values of α and β under different ratios have no differences. Therefore, we only report the results for the ratio of 4:4.

This result also provides the trustworthiness of the model interpretability. In the temporal domain, we notice that α remains relatively stable in different seasons, while β varies notably. This is primarily caused by foliage density changes.

5.4 Gateway Coverage Estimation

In this section, we evaluate the ESP estimation error using newly collected data from a new almond orchard. To estimate the gateway coverage, we collected data in a new manner as illustrated in Figure 30. The orchard was divided into multiple grids with an equal size of 19.2×19.2 m, resulting in a total of 8×8 grids. The transmission settings were kept the same as in the testbed. We collected 40 packets at each grid and used the average ESP of the received 40 packets as the ESP ground truth.

ESP Estimation: Figure 31(a) displays the average ESP measurements at each grid, demonstrating that ESP decreases as communication distance increases. To predict ESP values, we used the fitted parameters for the three models in the testbed. Figure 31(b)–(d) depicts the estimated ESP with Log, LLog, and *FLog* models. The Log model typically underestimates ESP, producing a darker blue, whereas the LLog model tends to overestimate ESP, resulting in a lighter blue. The generated ESP map using *FLog* is the most similar to the ground truth, indicating the lowest ESP estimation error.

PDR Estimation: PDR can be used as an indicator of the gateway coverage map. If PDR is greater than 80% [71, 74, 76], then we consider the grid to be covered by the gateway for a specific

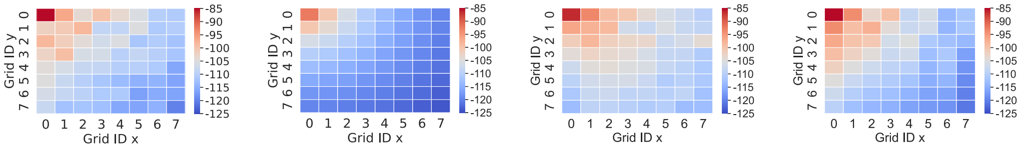

(a) ESP groundtruth (b) Log model (c) LLog model (d) *FLog* model

Fig. 31. ESP prediction results of three models in an almond orchard with 8 × 8 grids.

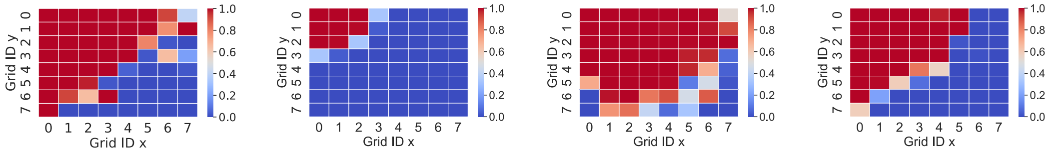

(a) PDR groundtruth (b) Log model (c) LLog model (d) *FLog* model

Fig. 32. The PDRs predicted by three models in an almond orchard with 8 × 8 grids.

SF. We also compute the ground truth of the PDR in each grid by dividing the number of correctly received packets by the total number of sent packets.

The results in Figure 32 show that SF7 can cover a large portion of the grids with a PDR of 100%. *FLog* achieves the average estimation error of 0.14, significantly lower than 0.26 and 0.46 of Log and LLog. Log underestimates the ESP of the received signal, ending up estimating that only eight grids can be covered, while LLog overestimates the received ESP, predicting that the gateway can cover almost all grids.

Reducing Construction Cost of Gateways: Given the cost of building a gateway with a height of 10 m consuming $15,400, building fewer gateways while maintaining reliable link quality would be advantageous. We use the above almond orchard with a 10-acre orchard as an example. *FLog* suggests only two gateways with a height of 10 m to cover all nodes and it ends up with communication failure. In contrast, Log suggests using seven gateways, which would increase the cost of building gateways to 107,800 dollars. However, LLog suggests using only one gateway but with communication failure in approximately 20% of the area. Such failures can lead to water waste or yield drop, negatively affecting the performance of many smart agricultural applications [17, 18, 33].

5.5 Computational Efficiency

FLog is generally efficient in computation, due to its interpretabilty. Specifically, PLE fitting and link quality calculation can be finished in 89 ms. The largest computation workload lies in the sampling process, as shown in Figure 9. The total time is proportional to the number of sampling points, which is positively correlated with $1/p\_gap$ and N_{ref} in Tables 2 and 3 and depends on CPU performance. In our implementation, the average sampling time for all 56 sensor locations in Section 5.2 is 97.1 s, which is satisfactory for the requirements, since resampling is conducted only for long-term shape changes.

6 Related Work

Modeing LoRa Link Quality: There have been several empirical studies conducted on the LoRa link quality [7–9, 11, 16, 35, 48, 54, 63, 65, 67]. For example, Adrian et al. [75] select locations of sensors and gateways to provide a LoS signal propagation path in FFZ. Demetri et al. [16] utilize remote sensing to quantitatively analyze the composition of land covers along LoRa links. Based on the dominant land-cover type along the link, they decide the right version of the Okumura-Hata model from two variants [28, 42, 46]. However, their method is not applicable in orchard scenarios. (1) Since orchards typically only have one type of land cover (i.e., trees), their method will ignore local spatial shadowing features such as the amount of space blocked by trees between the sensor nodes and the gateway. (2) The Urban model has deterministic parameters that are empirically fitted for cellular signals, which are typically received by base stations with high antenna heights, unlike LoRa gateways used in orchards.

Extensive measurements [9, 11, 48, 65, 73] have been conducted in various environments, such as indoor, urban, rural, and multi-floor buildings. Based on these measurements, empirical path loss models have been derived. Although these models perform well on their collected data, they do not consider the unique features of orchards, e.g., large deviations of the received signal powers in different directions that cannot be modeled via satellite images. *FLog* is a model based on FFZ theory, which can capture the wireless signal propagation mediums in orchards through 3D modeling.

Foliage Effect on Wireless Signals: The foliage has been observed to have a pronounced influence on link quality [30]. Numerous empirical foliage loss models have been introduced, including the Weissberger model [62], the ITU-R model [45], and the COST235 model [27]. However, implementing these models in orchards poses challenges for several reasons. First, they operate over different frequency bands, resulting in varying attenuation levels. Second, a majority of these models are deterministic, lacking flexible parameters to suit diverse orchard scenarios. Third, their representations of foliage are rather simplistic (e.g., assumed to be uniformly distributed in space), making them ill suited for handling significant signal power variations across different directions.

The two-ray ground-reflection model [78] is tailored for open environments with a direct LOS path between the transmitter and receiver. However, introducing foliage complicates the signal propagation paths, rendering this model unsuitable for the orchard context.

Furthermore, some models, inspired by the classical multi-wall-multi-floor indoor propagation paradigm [37], have considered the foliage effect. For instance, Gomez et al. [24] leverage a neural network to predict path loss across a foliage barrier, accounting for barrier thickness and vegetation density. Nevertheless, in actual orchard setups, foliage does not adhere to fixed-thickness wall models. Anzum et al. [6] statistically evaluate the attenuation induced by trunks and canopies along the transmission path. Their assumptions align with the preliminary LLog model and exclusively evaluate scenarios where trees lie directly between the transmitter and receiver. To summarize, while the multi-wall multi-floor model provides insightful perspectives for indoor settings, it fails to capture the intricate spatial dynamics of orchards. Contrarily, *FLog* gauges link quality by taking into account both the surrounding trees and the open spaces within FFZ.

LaPS [15] leverages remote sensing and LiDAR to locate trunks in forests and profile the canopy size of each tree. Then it uses multi-regression to get the shadowing parameters of each tree in the rectangular area along the path. *FLog* advances by utilizing the FFZ to judge the involvement of each canopy and mitigating the LiDAR scanning by leveraging the tidy layout of orchards.

Empirical Studies on LoRa Links: Bor et al. [9] discovered that in rural areas, communication distance could extend up to 3 km if the gateway is placed on a 100 m tall building. Centenario et al. [11] quantified the number of LoRa gateways required for citywide communication coverage and found that LoRa coverage could span up to 2 km when the gateway is placed in a high-building area. This article presents experimental results that demonstrate a significant reduction in communication distances in orchards due to the large attenuation of signal strength when gateways are deployed at limited heights. Cattani et al. [10] conducted experiments in indoor, outdoor, and underground settings and found that link reliability varied with environmental changes such as temperature. Voigt et al. [61] conducts simulations to analyze the influence of the in-network interference [14] from the other LoRa networks working over the same deployment area. The authors conclude that deploying additional gateways can make sure that all LoRa nodes are within the communication coverage of one of them. Orestis et al. [22] constructs the coverage probability by considering the ALOHA protocol, where the collisions happen if two packets with the same frequency channel and SF arrive at the gateway simultaneously. *FLog* develops a path loss propagation model for the orchard, paralleling research in these models.

Hakim et al. recognized the Fresnel zone non-clearance effect caused by low antenna height as a major component for obstacle loss, but lack a comprehensive approach for FFZ modeling [26]. FLog provides an in-depth analysis of LoRa signal propagation in orchards, culminating in a sophisticated path loss propagation model grounded in the FFZ.

7 Conclusion

This article presents *FLog*, a propagation model for LoRa signals in orchards. We first investigated the propagation characteristics of LoRa signals in orchards, revealing strong diffraction caused by trees and the ground. To capture these features, *FLog* estimates link quality by calculating the PLE in the Log-Normal Shadowing model for any pair of nodes and gateway using the FFZ theory. Extensive experiments demonstrate the effectiveness of our model.

Acknowledgments

We thank our editors and reviewers for their constructive comments.

References

[1] LoRa Packet Logger. 2017. Retrieved from https://github.com/Lora-net/lora_gateway. (2017).

[2] Semtech SX1276 Datasheet. 2020. Retrieved from https://www.semtech.com/products/wireless-rf/lora-transceivers/sx1276

[3] Arduino Uno Rev3. 2021. Retrieved from https://store-usa.arduino.cc/products/arduino-uno-rev3/?selectedStore=us

[4] Artifacts of FLog. 2023. Retrieved from https://github.com/ycucm/Flog

[5] Sayed Saad Afzal, Atsutse Kludze, Subhajit Karmakar, Ranveer Chandra, and Yasaman Ghasempour. 2023. AgriTera: Accurate non-invasive fruit ripeness sensing via sub-terahertz wireless signals. In *Proceedings of the ACM Annual International Conference on Mobile Computing and Networking (MobiCom'23)*.

[6] Rabeya Anzum, Mohamed Hadi Habaebi, Md Rafiqul Islam, Galang P. N. Hakim, Mayeen Uddin Khandaker, Hamid Osman, Sultan Alamri, and Elrashed AbdElrahim. 2022. A multiwall path-loss prediction model using 433 MHz LoRaWAN frequency to characterize foliage's influence in a Malaysian palm oil plantation environment. *Sensors* 22, 14 (2022), 5397.

[7] Iury da S. Batalha, Andréia Vanessa Rodrigues Lopes, Wirlan Gomes Lima, Yuri H. S. Barbosa, Miércio Cardoso De Alcântara Neto, Fabricio J. B. Barros, and Gervásio P. S. Cavalcante. 2022. Large-scale modeling and analysis of uplink and downlink channels for LoRa technology in suburban environments. *IEEE IoT J.* 9, 23 (2022), 24477–24491.

[8] Giulio Maria Bianco, Romeo Giuliano, Gaetano Marrocco, Franco Mazzenga, and Abraham Mejia-Aguilar. 2020. LoRa system for search and rescue: Path-loss models and procedures in mountain scenarios. *IEEE IoT J.* 8, 3 (2020), 1985–1999.

[9] Martin C. Bor, Utz Roedig, Thiemo Voigt, and Juan M. Alonso. 2016. Do LoRa low-power wide-area networks scale?. In *Proceedings of the International ACM Conference on Modeling Analysis and Simulation of Wireless and Mobile Systems (MSWiM'16)*.

[10] Marco Cattani, Carlo Alberto Boano, and Kay Römer. 2017. An experimental evaluation of the reliability of LoRa long-range low-power wireless communication. *J. Sens. Actuat. Netw.* 6, 2 (2017), 7.

[11] Marco Centenaro, Lorenzo Vangelista, Andrea Zanella, and Michele Zorzi. 2016. Long-range communications in unlicensed bands: The rising stars in the IoT and smart city scenarios. *IEEE Wireless Commun.* 23, 5 (2016), 60–67.

[12] Yuning Chen, Kang Yang, Zhiyu An, Brady Holder, Luke Paloutzian, Khaled M. Bali, and Wan Du. 2024. MARLP: Time-series forecasting control for agricultural managed aquifer recharge. In *Proceedings of the 30th ACM SIGKDD Conference on Knowledge Discovery and Data Mining (KDD'24)*.

[13] Tuan Dang, Trung Tran, Khang Nguyen, Tien Pham, Nhat Pham, Tam Vu, and Phuc Nguyen. 2022. ioTree: A battery-free wearable system with biocompatible sensors for continuous tree health monitoring. In *Proceedings of the ACM Annual International Conference on Mobile Computing and Networking (MobiCom'22)*.

[14] Clement Demeslay, Philippe Rostaing, and Roland Gautier. 2021. Theoretical performance of LoRa system in multipath and interference channels. *IEEE IoT J.* 9, 9 (2021), 6830–6843.

[15] Silvia Demetri, Gian Pietro Picco, and Lorenzo Bruzzone. 2019. LaPS: LiDAR-assisted placement of wireless sensor networks in forests. *ACM Trans. Sens. Netw.* 15, 2 (2019), 1–40.

[16] Silvia Demetri, Marco Zúñiga, Gian Pietro Picco, Fernando Kuipers, Lorenzo Bruzzone, and Thomas Telkamp. 2019. Automated estimation of link quality for LoRa: A remote sensing approach. In *Proceedings of the ACM/IEEE International Conference on Information Processing in Sensor Networks (IPSN'19)*.

[17] Xianzhong Ding and Wan Du. 2022. DRLIC: Deep reinforcement learning for irrigation control. In *Proceedings of the ACM/IEEE International Conference on Information Processing in Sensor Networks (IPSN'22)*.

[18] Xianzhong Ding and Wan Du. 2024. Optimizing irrigation efficiency using deep reinforcement learning in the field. *ACM Trans. Sens. Netw.* 20, 4 (2024), 1–34.

[19] Wan Du, Jansen Christian Liando, Huanle Zhang, and Mo Li. 2015. When pipelines meet fountain: Fast data dissemination in wireless sensor networks. In *Proceedings of the ACM Conference on Embedded Networked Sensor Systems (SenSys'15)*.

[20] Tallal Elshabrawy and Joerg Robert. 2018. Closed-form approximation of LoRa modulation BER performance. *IEEE Commun. Lett.* 22, 9 (2018), 1778–1781.

[21] Amalinda Gamage, Jansen Christian Liando, Chaojie Gu, Rui Tan, and Mo Li. 2020. LMAC: Efficient carrier-sense multiple access for LoRa. In *Proceedings of the ACM Annual International Conference on Mobile Computing and Networking (MobiCom'20)*.

[22] Orestis Georgiou and Usman Raza. 2017. Low power wide area network analysis: Can LoRa scale? *IEEE Wireless Commun. Lett.* 6, 2 (2017), 162–165.

[23] Andrea Goldsmith. 2005. *Wireless Communications*. Cambridge University Press.

[24] Paula Gómez-Pérez, Marcos Crego-García, Iñigo Cuiñas, and Rafael F. S. Caldeirinha. 2017. Modeling and inferring the attenuation induced by vegetation barriers at 2G/3G/4G cellular bands using Artificial Neural Networks. *Measurement* 98 (2017), 262–275.

[25] Xiuzhen Guo, Longfei Shangguan, Yuan He, Nan Jing, Jiacheng Zhang, Haotian Jiang, and Yunhao Liu. 2022. Saiyan: Design and implementation of a low-power demodulator for {LoRa} backscatter systems. In *Proceedings of the USENIX Symposium on Networked Systems Design and Implementation (NSDI'22)*.

[26] Galang P. N. Hakim, Mohamed Hadi Habaebi, Siti Fauziah Toha, Mohamed Rafiqul Islam, Siti Hajar Binti Yusoff, Erry Yulian Triblas Adesta, and Rabeya Anzum. 2022. Near ground pathloss propagation model using adaptive neuro fuzzy inference system for wireless sensor network communication in forest, jungle and open dirt road environments. *Sensors* 22, 9 (2022), 3267.

[27] MPM Hall. 1993. COST project 235 activities on radiowave propagation effects on next-generation fixed-service terrestrial telecommunication systems. In *Proceedings of the IET International Conference on Antennas and Propagation (ICAP'93)*.

[28] Masaharu Hata. 1980. Empirical formula for propagation loss in land mobile radio services. *IEEE Trans. Vehic. Technol.* 29, 3 (1980), 317–325.

[29] Ningning Hou, Xianjin Xia, and Yuanqing Zheng. 2023. Jamming of LoRa PHY and countermeasure. *ACM Trans. Sens. Netw.* 19, 4 (2023), 1–27.

[30] M. S. Karaliopoulos and F.-N. Pavlidou. 1999. Modelling the land mobile satellite channel: A review. *Electr. Commun. Eng. J.* 11, 5 (1999), 235–248.

[31] Abhishek Khanna and Sanmeet Kaur. 2019. Evolution of Internet of Things (IoT) and its significant impact in the field of Precision Agriculture. *Comput. Electr. Agric.* 157 (2019), 218–231.

[32] kubernets. n.d.. Production-Grade Container Orchestration. Retrieved from https://kubernetes.io/

[33] Fudong Lin, Kaleb Guillot, Summer Crawford, Yihe Zhang, Xu Yuan, and Nian-Feng Tzeng. 2024. An open and large-scale dataset for multi-modal climate change-aware crop yield predictions. In *Proceedings of the 30th ACM SIGKDD Conference on Knowledge Discovery and Data Mining (KDD'24)*.

[34] Yuxiang Lin, Wei Dong, Yi Gao, and Tao Gu. 2021. Sateloc: A virtual fingerprinting approach to outdoor LoRa localization using satellite images. *ACM Trans. Sens. Netw.* 17, 4 (2021), 1–28.

[35] Li Liu, Yuguang Yao, Zhichao Cao, and Mi Zhang. 2021. DeepLoRa: Learning accurate path loss model for long distance links in LPWAN. In *Proceedings of the IEEE International Conference on Computer Communications (INFOCOM'21)*.

[36] Yilin Liu, Shijia Zhang, Mahanth Gowda, and Srihari Nelakuditi. 2022. Leveraging the properties of mmwave signals for 3d finger motion tracking for interactive iot applications. In *Proceedings of the ACM on Measurement and Analysis of Computing Systems*. ACM, New York, NY, 1–28.

[37] Matthias Lott and Ingo Forkel. 2001. A multi-wall-and-floor model for indoor radio propagation. In *Proceedings of the IEEE VTS 53rd Vehicular Technology Conference*, Vol. 1. IEEE, 464–468.

[38] Michael Marcus and Bruno Pattan. 2005. Millimeter wave propagation: Spectrum management implications. *IEEE Microw. Mag.* 6, 2 (2005), 54–62.

[39] Luoyu Mei, Zhimeng Yin, Shuai Wang, Xiaolei Zhou, Taiwei Ling, and Tian He. 2024. ECRLoRa: LoRa packet recovery under low SNR via edge–cloud collaboration. *ACM Trans. Sens. Netw.* 20, 2 (2024), 1–25.

[40] Manuel Eugenio Morocho-Cayamcela, Martin Maier, and Wansu Lim. 2020. Breaking wireless propagation environmental uncertainty with deep learning. *IEEE Trans. Wireless Commun.* 19, 8 (2020), 5075–5087.

[41] Han Na and Thomas F. Eibert. 2022. A huygens' principle based ray tracing method for diffraction calculation. In *Proceedings of the IEEE European Conference on Antennas and Propagation (EuCAP'22).*

[42] Yoshihisa Okumura. 1968. Field strength and its variability in VHF and UHF land-mobile radio service. *Rev. Electr. Commun. Lab.* 16 (1968), 825–873.

[43] Michele Preti, François Verheggen, and Sergio Angeli. 2021. Insect pest monitoring with camera-equipped traps: Strengths and limitations. *J. Pest Sci.* 94, 2 (2021), 203–217.

[44] John G. Proakis and Masoud Salehi. 2008. *Digital Communications, 5th Edition.* McGraw–Hill.

[45] International Telecommunication Union Radiocommunication. 2001. Attenuation in vegetation. (2001).

[46] Theodore S. Rappaport, et al. 1996. *Wireless Communications: Principles and Practice.* Vol. 2. Prentice Hall, New Jersey.

[47] Yidong Ren, Amalinda Gamage, Li Liu, Mo Li, Shigang Chen, Younsuk Dong, and Zhichao Cao. 2024. Sateriot: High-performance ground-space networking for rural iot. In *Proceedings of the 30th Annual International Conference on Mobile Computing and Networking.* 755–769.

[48] Yidong Ren, Li Liu, Chenning Li, Zhichao Cao, and Shigang Chen. 2022. Is LoRaWAN really wide? Fine-grained LoRa link-level measurement in an urban environment. In *Proceedings of the IEEE International Conference on Network Protocols (ICNP'22).*

[49] Yidong Ren, Wei Sun, Jialuo Du, Huaili Zeng, Younsuk Dong, Mi Zhang, Shigang Chen, Yunhao Liu, Tianxing Li, and Zhichao Cao. 2024. Demeter: Reliable cross-soil LPWAN with low-cost signal polarization alignment. In *Proceedings of the 30th Annual International Conference on Mobile Computing and Networking.* 230–245.

[50] Pedro M. Santos, Traian E. Abrudan, Ana Aguiar, and Joao Barros. 2014. Impact of position errors on path loss model estimation for device-to-device channels. *IEEE Trans. Wireless Commun.* 13, 5 (2014), 2353–2361.

[51] Scipy. Non-linear Least-Square Algorithm. Retrieved from https://docs.scipy.org/doc/scipy/reference/generated/scipy.optimize.least_squares.html

[52] Richard L. Snyder. 1984. California irrigation management information system. *Am. Potato J.* 61 (1984), 229–234.

[53] Tossaporn Srisooksai, Kamol Kaemarungsi, Junichi Takada, and Kentaro Saito. 2019. Path loss measurement and prediction in outdoor fruit orchard for wireless sensor network at 2.4 GHz band. *Progr. Electromagnet. Res. C* 90 (2019), 237–252.

[54] Jothi Prasanna Shanmuga Sundaram, Wan Du, and Zhiwei Zhao. 2019. A survey on LoRa networking: Research problems, current solutions, and open issues. *IEEE Commun. Surv. Tutor.* 22, 1 (2019), 371–388.

[55] Wankai Tang, Ming Zheng Chen, Xiangyu Chen, Jun Yan Dai, Yu Han, Marco Di Renzo, Yong Zeng, Shi Jin, Qiang Cheng, and Tie Jun Cui. 2020. Wireless communications with reconfigurable intelligent surface: Path loss modeling and experimental measurement. *IEEE Trans. Wireless Commun.* 20, 1 (2020), 421–439.

[56] RAKwireless Technology. RAK831 Pilot Gateway Product Specification V1.3. n.d. Retrieved from https://www.thethingsnetwork.org/docs/gateways/rak831/

[57] Yas Hosseini Tehrani, Arash Amini, and Seyed Mojtaba Atarodi. 2020. A tree-structured LoRa network for energy efficiency. *IEEE IoT J.* 8, 7 (2020), 6002–6011.

[58] Saul A. Torrico, Henry L. Bertoni, and Roger H. Lang. 1998. Modeling tree effects on path loss in a residential environment. *IEEE Trans. Antennas Propagat.* 46, 6 (1998), 872–880.

[59] United States Department of Agriculture National Agricultural Statistics Service. 2021. California Almond Acreage Report. Retrieved from https://www.almonds.com/sites/default/files/2022-04/2021_NASS_Acreage_Report.pdf

[60] United States Department of Agriculture, National Agricultural Statistics Service. n.d. California Agricultural Production Statistics. Retrieved from https://www.cdfa.ca.gov/Statistics/

[61] Thiemo Voigt, Martin Bor, Utz Roedig, and Juan Alonso. 2016. Mitigating inter-network interference in LoRa networks. arXiv:1611.00688. Retrieved from https://arxiv.org/abs/1611.00688

[62] Mark A. Weissberger. 1982. *An Initial Critical Summary of Models for Predicting the Attenuation of Radio Waves by Trees.* Technical Report. Electromagnetic Compatibility Analysis Center Annapolis MD.

[63] Zongxing Xie and Fan Ye. 2022. Self-calibrating indoor trajectory tracking system using distributed monostatic radars for large scale deployment. In *Proceedings of the 9th ACM International Conference on Systems for Energy-Efficient Buildings, Cities, and Transportation.* 188–197.

[64] Jie Xiong, Karthikeyan Sundaresan, and Kyle Jamieson. 2015. Tonetrack: Leveraging frequency-agile radios for time-based indoor wireless localization. In *Proceedings of the ACM Annual International Conference on Mobile Computing and Networking (MobiCom'15).*

[65] Weitao Xu, Jun Young Kim, Walter Huang, Salil S. Kanhere, Sanjay K. Jha, and Wen Hu. 2019. Measurement, characterization, and modeling of lora technology in multifloor buildings. *IEEE IoT J.* 7, 1 (2019), 298–310.

[66] Yifei Xu, Yuning Chen, Xumiao Zhang, Xianshang Lin, Pan Hu, Yunfei Ma, Songwu Lu, Wan Du, Zhuoqing Mao, Ennan Zhai, et al. 2024. CloudEval-YAML: A practical benchmark for cloud configuration generation. (unpublished).

[67] Kang Yang, Yuning Chen, Xuanren Chen, and Wan Du. 2023. Link quality modeling for LoRa networks in orchards. In *Proceedings of the 22nd ACM/IEEE Conference on Information Processing in Sensor Networks (IPSN'23).*

[68] Kang Yang, Yuning Chen, and Wan Du. 2024. OrchLoc: In-orchard localization via a single LoRa gateway and generative diffusion model-based fingerprinting. In *Proceedings of the 22nd ACM International Conference on Mobile Systems, Applications, and Services (MobiSys'24).*

[69] Kang Yang and Wan Du. 2022. LLDPC: A low-density parity-check coding scheme for LoRa networks. In *Proceedings of the 20th ACM Conference on Embedded Networked Sensor Systems (SenSys'22).*

[70] Kang Yang and Wan Du. 2024. A low-density parity-check coding scheme for LoRa networking. *ACM Trans. Sens. Netw.* 20, 4 (2024), 1–29.

[71] Kang Yang, Miaomiao Liu, and Wan Du. 2024. RALoRa: Rateless-enabled link adaptation for LoRa networking. *IEEE/ACM Trans. Netw.* 32, 4 (2024), 3392–3407.

[72] Kun Yang, Andreas F. Molisch, Torbjörn Ekman, Terje Røste, and Marion Berbineau. 2019. A round earth loss model and small-scale channel properties for open-sea radio propagation. *IEEE Trans. Vehic. Technol.* 68, 9 (2019), 8449–8460.

[73] Jane Yen, Jianfeng Wang, Sucha Supittayapornpong, Marcos A. M. Vieira, Ramesh Govindan, and Barath Raghavan. 2020. Meeting slos in cross-platform nfv. In *Proceedings of the ACM International Conference on Emerging Networking EXperiments and Technologies (CoNEXT'20).*

[74] Jennifer Yick, Biswanath Mukherjee, and Dipak Ghosal. 2008. Wireless sensor network survey. *Comput. Netw.* 52, 12 (2008), 2292–2330.

[75] Adrian Zarnescu, Razvan Ungurelu, Mihai Secere, Gaudentiu Varzaru, and Bogdan Mihailescu. 2020. Implementing a large LoRa network for an agricultural application. In *Proceedings of the IEEE International Conference on Energy Efficiency & Agricultural Engineering (EE&AE'20).*

[76] Jerry Zhao and Ramesh Govindan. 2003. Understanding packet delivery performance in dense wireless sensor networks. In *Proceedings of the ACM Conference on Embedded Networked Sensor Systems (SenSys'03).*

[77] Xiaopeng Zhao, Zhenlin An, Qingrui Pan, and Lei Yang. 2023. NeRF^2: Neural radio-frequency radiance fields. In *Proceedings of the ACM Annual International Conference on Mobile Computing and Networking (MobiCom'23).*

[78] Erich Zöchmann, Ke Guan, and Markus Rupp. 2017. Two-ray models in mmWave communications. In *Proceedings of the IEEE International Workshop on Signal Processing Advances in Wireless Communications (SPAWC'17).*

Received 20 February 2024; revised 11 November 2024; accepted 12 January 2025